Coreline Criteria for Inertial Particle Motion

Irene Baeza Rojo and Tobias Günther

Abstract Dynamical systems, such as the second-order ODEs that govern the motion of finite-sized objects in fluids, describe the evolution of a state by a trajectory living in a high-dimensional phase space. The high dimensionality leads to visualization challenges and, for the case of inertial particles, multiple models exist that pose different assumptions. In this paper, we thoroughly address the extraction of a specific feature, namely the vortex corelines of inertial particles. Based on a general template model that comprises two of the most commonly used inertial particle ODEs, we first transform their high-dimensional tangent vector field into a Galilean reference frame in which the observed inertial particle flow becomes as steady as possible. In the optimal frame, we derive first-order and second-order vortex coreline criteria, allowing us to extract straight and bent inertial vortex corelines using 3D and 6D parallel vectors operators, respectively. With this, we generalize existing work in multiple ways: not only do we handle two inertial particle models at once, we extend the concept of second-order vortex corelines to the inertial case and make them Galilean-invariant by deriving the criteria from a steady reference frame, rather than from a geometric characterization.

1 Introduction

In this paper, we study the vortical motion of finite-sized objects in time-dependent fluids, such as sand particles in air or bubbles in water. Such vortex dynamics occur

Irene Baeza Rojo
Department of Computer Science, ETH Zürich
e-mail: irene.baeza@inf.ethz.ch

Tobias Günther
Department of Computer Science, ETH Zürich
e-mail: tobias.guenther@inf.ethz.ch
Present address: FAU Erlangen-Nürnberg

for instance when helicopters approach the ground [1, 2, 3], in the detection of marine debris [4], and in the formation of rain [5]. Previous methods [6, 7] used an aerosol particle model that had only one degree of freedom. We extend the vortex coreline extraction in unsteady flows to a more general inertial particle model that captures a wider spectrum of density ratios between the particle and the surrounding medium. Using a generalized description that contains both models as special cases, we develop a first-order and a second-order feature extractor based on Sujudi-Haimes [8] and Roth and Peikert [9], respectively. While the first-order extraction can be carried out with standard 3D parallel vectors extractors [10], the second-order criterion requires the search for 6D parallel vectors in a high-dimensional 6D space, for which we use a Bézier-based subdivision with subsequent Newton iterations. Instead of deriving the vortex criteria only from a geometric point of view in space-time [6], we extract the vortex corelines in local Galilean reference frames in which the flow field becomes as steady as possible [11, 12]. When it comes to vortex coreline extraction, there are two orthogonal concepts: the shape of the coreline, and the motion of the coreline. While previous work [7] concentrated on the motion, our focus is on the shape of the coreline, as we search for straight and curved corelines. Assuming that vortices perform Galilean transformations, we transform our flow into a reference frame in which the time partial derivative vanishes by optimizing for a Galilean transformation. In the optimal frame, the resulting vortex extraction methods therefore become Galilean invariant. In summary, we contribute:

- a generalization of the inertial vortex coreline criterion of Günther and Theisel [6] to a more general particle model,
- and a second-order criterion that extracts bent inertial vortex corelines, for which we generalize Roth and Peikert [9].

Notation. In the following, we denote scalars s in italic letters, vectors $\mathbf{v}$ are bold and matrices $\mathbf{J}$ are bold upper-case letters. Throughout the chapter, $\mathbf{I}$ denotes the identity matrix. Quantities in the space-velocity domain are denoted with a tilde $\tilde{\mathbf{v}}$.

2 Related Work

2.1 Galilean Invariance

Galilean invariance is a desirable formal property that the measure of a feature might have. If a measure (such as a vortex measure) is Galilean invariant, then it does not change under Galilean transformations of the reference frame [23]. Formally, a Galilean transformation maps a point $(\mathbf{x}, t)$ to the point $(\mathbf{x}^*, t^*)$:

$$\mathbf{x}^* = \mathbf{x} + \mathbf{c} + t\,\mathbf{d}\,, \qquad t^* = t + a\,, \tag{1}$$

where $\mathbf{c}$ and $\mathbf{d}$ are constant vectors and a is a constant scalar. Accordingly, a vector field $\mathbf{u}(\mathbf{x}, t)$ is transformed to:

$$\mathbf{u}^*(\mathbf{x}^*, t^*) = \mathbf{u}(\mathbf{x}, t) + \mathbf{d} \tag{2}$$

$$= \mathbf{u}(\mathbf{x}^* - \mathbf{c} - t\,\mathbf{d}, t^* - a) + \mathbf{d}\,, \tag{3}$$

which follows from differentiation of Eq. (1) to consider how the tangent of a pathline $\frac{\mathrm{d}\mathbf{x}^*(t^*)}{\mathrm{d}t} = \mathbf{u}^*(\mathbf{x}^*, t^*)$ is transformed. A measure $\mathcal{M}$ is Galilean invariant if it gives the same result at both locations in the accordingly transformed vector fields, i.e., $\mathcal{M}(\mathbf{x}, \mathbf{u}, t) = \mathcal{M}(\mathbf{x}^*, \mathbf{u}^*, t^*)$. For example, applying the ∇ operator to both sides of Eq. (2) shows that the Jacobian is Galilean invariant, since $\nabla\mathbf{u}^*(\mathbf{x}^*, t^*) = \nabla\mathbf{u}(\mathbf{x}, t)$, given that $\nabla\mathbf{d} = \mathbf{0}$ because $\mathbf{d}$ is constant.

Since the motion of the reference frame and the motion of the feature are relative to each other, Galilean invariance not only guarantees that measures do not change under motions of the observer; they also do not change when the feature itself is moving. In other words, a Galilean invariant vortex measure will give the same result if vortices move with constant speed in a constant direction, which ultimately allows us to extract moving vortices.

2.2 Inertial Particle Motion

The motion of finite-sized particles in fluids can be described by a second-order ODE, which can be rephrased into a coupled first-order ODE [6]. Depending on the possible simplifying assumptions, different equations of motion are possible, which resulted in a number of different particle models [13, 14, 15, 16]. Throughout this work, we use two inertial particle models. The underlying fluid flow is described by the n-d unsteady vector field $\mathbf{u}(\mathbf{x}, t) : \mathbb{R}^n \times \mathbb{R} \to \mathbb{R}^n$.

Model 1. The first model was described by Crowe et al. [13] and considers small particles in air. With $\mathbf{g}$ being the gravity vector, it reads:

$$\tilde{\mathbf{v}}(\mathbf{x}, \mathbf{v}, t) = \begin{pmatrix} \mathbf{v} \\ \frac{\mathbf{u}(\mathbf{x},t)-\mathbf{v}}{r} + \mathbf{g} \end{pmatrix}\,. \tag{4}$$

The particle response time $r = \frac{d_p^2 \rho_p}{18\mu}$ determines how quickly an inertial particle aligns its own velocity $\mathbf{v}$ with the underlying air flow $\mathbf{u}(\mathbf{x}, t)$, where d_p is the particle size, ρ_p is the particle density and μ is the viscosity of the underlying air flow. The smaller r is, the lighter the particle, with tracer particles arising in the limit for $r \to 0$. This particle model has frequently been used to model the motion of sand particles in air [17, 18, 1, 19, 3], and assumes that particles are spherical, very small, and have a much higher density than the surrounding air.

Model 2. The second model was used by Haller [14] and distinguishes between aerosols and bubbles, based on the density ratio $R = 2\rho_f/(\rho_f + 2\rho_p)$, where ρ_f is the fluid density and ρ_p is the particle density. For $R < 2/3$ we have aerosols ($\rho_p > \rho_f$, e.g., sand particles in air), for $R = 2/3$ we obtain neutrally buoyant particles ($\rho_p = \rho_f$) and for $R > 2/3$ the motion of bubbles ($\rho_p < \rho_f$) is modeled:

$$\tilde{\mathbf{v}}(\mathbf{x}, \mathbf{v}, t) = \begin{pmatrix} \mathbf{v} \\ \frac{R}{St}(\mathbf{u}(\mathbf{x}, t) - \mathbf{v}) + \frac{3R}{2}\frac{D\mathbf{u}(\mathbf{x},t)}{Dt} + \left(1 - \frac{3R}{2}\right)\mathbf{g} \end{pmatrix}, \tag{5}$$

where $\frac{D\mathbf{u}(\mathbf{x},t)}{Dt} = \mathbf{J}\mathbf{u} + \mathbf{u}_t$ is the material derivative of the flow, i.e., the acceleration, and $\mathbf{u}_t = \frac{\partial \mathbf{u}(\mathbf{x},t)}{\partial t}$ is the time partial derivative of the flow. The Stokes number St determines the amount of inertia, with $St \to 0$ approaching the behavior of tracer particles. This model and its variations, such as gravity-free environments or neutrally buoyant particles, have been used extensively in the fluid dynamics literature [20, 21, 22, 14, 15].

2.3 Vortex Corelines of Massless Flows

Vortex coreline definitions have evolved over the last two decades, adding more and more generality. We mainly focus on the methods that led up to this paper. For a more comprehensive overview, we refer to the recent survey of Günther and Theisel [23].

Corelines in Steady Flows. The earliest influential algorithms were built for steady flows. Globus et al. [24] traced streamlines from attracting and repelling foci and Sujudi and Haimes [8] introduced the reduced velocity criterion. In the presence of complex eigenvalues in the Jacobian $\mathbf{J} = \nabla\mathbf{u}$, let $\mathbf{e}$ be the single eigenvector with a real eigenvalue. Sujudi and Haimes requested that the projection of the velocity along vector $\mathbf{e}$ is zero: $\mathbf{u} - (\mathbf{u}^\mathrm{T}\mathbf{e})\,\mathbf{e} = \mathbf{0}$. In other words, the flow exactly on the vortex coreline is not in the swirling plane, but only moves forward. Peikert and Roth [10] introduced the parallel vectors (PV) operator, which returns for two vector fields the set of locations at which the two vector fields are parallel. With $\mathbf{u} \parallel \mathbf{e}$, the method of Sujudi-Haimes [8] can be rephrased in PV notation, which is often computed as $\mathbf{u} \parallel \mathbf{J}\,\mathbf{u}$. Other vortex coreline conditions, such as helicity extrema, vorticity extrema and λ_2 extrema, can likewise be expressed by the PV operator [10, 25].

Corelines in Unsteady Flows. Fuchs et al. [26] extended this reduced velocity criterion to unsteady flows by extracting $\mathbf{u} \parallel \mathbf{J}\,\mathbf{u} + \mathbf{u}_t$. Another approach was taken by Weinkauf et al. [27], who applied the reduced velocity criterion in space-time. Since there are, in space-time, two eigenvectors with real eigenvalue (one of them is zero), the flow vector $\mathbf{u}$ must be in the plane that is spanned by these two eigenvectors to not take part in the swirling plane. This co-planar vectors condition simplifies to the PV condition $\mathbf{u} - \mathbf{f} \parallel \mathbf{J}(\mathbf{u} - \mathbf{f})$, with $\mathbf{f}$ being the feature flow field [28]. Günther et al. [29] introduced a rotation invariant coreline condition. By linear optimization, rotating and translating reference frames have recently been extracted, in which the flow becomes steady [30, 31]. The idea is that, in the optimal frame, vortex features are no longer obscured by ambient motion. The solution must vary spatially, since no global observer exists for the entire domain [11, 12, 32]. While Günther and Theisel optimized the reference frame locally at each point in space-time, Hadwiger et al. [31] formulated the search for optimal reference frames as a global optimization problem, in which the

motion is described by an approximate Killing field. Note that a global optimization is infeasible for inertial particle motion, since this would require to discretize the entire seven-dimensional phase space. More recently, reference frame optimization has been extended to spatially-varying transformations, which opened a path to topology-based methods beyond vortices [33]. Günther and Theisel [34] have shown that the method of Weinkauf et al. [27] is optimal for vortices performing Galilean transformations. Other reference frame adjustments used flow decompositions [35, 36, 37], adjusted to Galilean-invariant extremal features [38] or used machine learning [39].

Second-order Corelines. The local coreline conditions above can all be classified as first-order methods, since they only involve first-order derivatives. For steady flows $\mathbf{u}(x, y, z)$, the method of Roth and Peikert [9] computes bent vortex corelines with

$$\mathbf{u} \parallel \mathbf{b} \quad \text{with} \quad \mathbf{b} = \frac{D}{Dt}(\mathbf{J}\mathbf{u}) = (\nabla\mathbf{J}\mathbf{u} + \mathbf{J}\mathbf{J})\,\mathbf{u}\,, \tag{6}$$

where $\nabla\mathbf{J}\mathbf{u} = \mathbf{J}_x u + \mathbf{J}_y v + \mathbf{J}_z w$. Note that this method is not Galilean invariant, even when calculating $\mathbf{b} = \frac{D}{Dt}(\mathbf{J}\mathbf{u} + \mathbf{u}_t)$, since the material derivative entails a multiplication with $\mathbf{u}$, which is not invariant. In this paper, we extend this approach to the high-dimensional vector field of inertial particles. When considered in a reference frame in which the flow is steady, the approach becomes reference frame invariant.

2.4 Vortex Corelines of Inertial Particles

For inertial particles, Günther and Theisel [6] proposed an inertial first-order vortex coreline criterion that is Galilean invariant. However, their condition is tailored to Model 1 and can only guarantee to correctly extract straight vortex corelines. To arrive at this condition, they followed a geometric construction [27].

The method was extended by Günther and Theisel [7] to handle more kinds of vortex motions, namely all smooth rotations and translations. For this, a linear optimization is needed that finds a reference frame in which the high-dimensional flow becomes as steady as possible. Then, the above method [6] is applied to find straight inertial vortex corelines. As before, the extractor was tailored to Model 1.

In this paper, we further extend the method of Günther and Theisel [6] in three ways. First, we derive vortex criteria not only for Model 1, but for a more general template that includes Model 1 and Model 2 as special cases. Second, we extend the method of Roth and Peikert [9] to derive a second-order vortex coreline criterion that extracts bent inertial vortex corelines. Third, instead of deriving the vortex criteria geometrically, we follow a reference frame centered approach, which is for both the first-order and second-order case Galilean invariant, and arrives for the special case of Model 1 at the same condition as [6]. This gives new insights on the mathematical properties of their solution.

3 Vortex Coreline Criteria for Inertial Particles

Our inertial vortex coreline criteria are fundamentally based on the observation of the time-dependent high-dimensional vector field in a reference frame in which the flow becomes steady. Since we concentrate on the shape of the corelines instead of the motion, we assume a Galilean transformation. Therefore, we first introduce Galilean reference frame transformations of inertial particles and derive the analytic solution to the optimal reference frame for both inertial particle models. Afterwards, we derive the inertial vortex coreline conditions that are applied in the optimal frame. We begin with first-order criteria in 2D, in 2D space-time, and in 3D. Afterwards, we introduce the second-order vortex coreline criterion that allows us to find bent corelines.

3.1 Generalized Inertial Particle Motion

Similar to Günther and Gross [40], we utilize a generalized template-based description of the particle motion, which allows us to express local properties of inertial particles for multiple models at once. Their template-based description introduces abstract variables that are assigned dependent on the particle model. While Günther and Gross generalized the high-dimensional Jacobian matrix $\tilde{\mathbf{J}}$, we generalize the underlying high-dimensional vector field $\tilde{\mathbf{v}}$ instead. Let κ be a constant scalar and $\mathbf{k}(\mathbf{x},t)$ be an n-d vector field. The change in particle position $\mathbf{x}$ and particle velocity $\mathbf{v}$ of an inertial particle are described by the high-dimensional vector field $\tilde{\mathbf{v}}(\mathbf{x},\mathbf{v},t)$:

$$\tilde{\mathbf{v}}(\mathbf{x},\mathbf{v},t) = \frac{\mathrm{d}}{\mathrm{d}t}\begin{pmatrix}\mathbf{x}\\ \mathbf{v}\end{pmatrix} = \begin{pmatrix}\mathbf{v}\\ \mathbf{k}(\mathbf{x},t) - \frac{\mathbf{v}}{\kappa}\end{pmatrix} . \tag{7}$$

Intuitively speaking, position $\mathbf{x}$ and velocity $\mathbf{v}$ are the two properties that are stored per particle. Then, the high-dimensional vector field $\tilde{\mathbf{v}}$ is the vector field in which inertial particle trajectories are traced as tangent curves. The high-dimensional Jacobian matrix $\tilde{\mathbf{J}} = \nabla\tilde{\mathbf{v}}$ contains the $\mathbf{x}$ and $\mathbf{v}$ partials as column vectors and becomes:

$$\tilde{\mathbf{J}}(\mathbf{x},\mathbf{v},t) = \left(\frac{\partial\tilde{\mathbf{v}}(\mathbf{x},\mathbf{v},t)}{\partial\mathbf{x}}, \frac{\partial\tilde{\mathbf{v}}(\mathbf{x},\mathbf{v},t)}{\partial\mathbf{v}}\right) = \begin{pmatrix}\mathbf{0} & \mathbf{I}\\ \nabla\mathbf{k}(\mathbf{x},t) & -\frac{1}{\kappa}\mathbf{I}\end{pmatrix} , \tag{8}$$

which can be used to locally analyze the behavior of inertial particles. By a suitable choice of κ and $\mathbf{k}(\mathbf{x},t)$, Eqs. (7) and (8) can describe inertial particle motion:

$$\text{Model 1}: \quad \kappa = r, \qquad \mathbf{k}(\mathbf{x},t) = \frac{\mathbf{u}(\mathbf{x},t)}{r} + \mathbf{g} , \tag{9}$$

$$\text{Model 2}: \quad \kappa = \frac{St}{R}, \quad \mathbf{k}(\mathbf{x},t) = \frac{R}{St}\mathbf{u}(\mathbf{x},t) + \frac{3R}{2}\frac{D\mathbf{u}(\mathbf{x},t)}{Dt} + \left(1 - \frac{3R}{2}\right)\mathbf{g} . \tag{10}$$

Galilean Transformation. Since inertial particle motion is described by a higher-dimensional vector field, we now consider how an inertial particle in the high-dimensional space changes under Galilean transformations. From Eqs. (1) and (2), we see how position $\mathbf{x}(t)$ and velocity $\mathbf{v}(t)$ of an inertial particle $\tilde{\mathbf{p}}(t) = \begin{pmatrix}\mathbf{x}(t)\\ \mathbf{v}(t)\end{pmatrix}$ are transformed to $\tilde{\mathbf{p}}^*(t)$:

$$\tilde{\mathbf{p}}^*(t) = \begin{pmatrix}\mathbf{x}^*(t)\\ \mathbf{v}^*(t)\end{pmatrix} = \begin{pmatrix}\mathbf{x}(t) + \mathbf{c} + t\,\mathbf{d}\\ \mathbf{v}(t) + \mathbf{d}\end{pmatrix} . \tag{11}$$

The above particle $\tilde{\mathbf{p}}^*$ moves tangentially in the high-dimensional vector field $\tilde{\mathbf{v}}^*$ that governs its motion. By differentiating Eq. (11), we consider the tangent of our particle at $(\mathbf{x}^*, \mathbf{v}^*)$ to see how the governing high-dimensional vector field is transformed

$$\tilde{\mathbf{v}}^* = \frac{\mathrm{d}\tilde{\mathbf{p}}^*}{\mathrm{d}t}_{|\mathbf{x}^*,\mathbf{v}^*} = \begin{pmatrix}\frac{\mathrm{d}\mathbf{x}(t)}{\mathrm{d}t} + \mathbf{d}\\ \frac{\mathrm{d}\mathbf{v}(t)}{\mathrm{d}t}\end{pmatrix} = \frac{\mathrm{d}\tilde{\mathbf{p}}}{\mathrm{d}t}_{|\mathbf{x},\mathbf{v}} + \begin{pmatrix}\mathbf{d}\\ \mathbf{0}\end{pmatrix} = \tilde{\mathbf{v}} + \begin{pmatrix}\mathbf{d}\\ \mathbf{0}\end{pmatrix} . \tag{12}$$

By inserting our generalized particle model from Eq. (7) into the Galilean transformed high-dimensional flow in Eq. (12), we obtain the transformed high-dimensional vector field that governs the inertial particle motion for both our considered models:

$$\tilde{\mathbf{v}}^* = \begin{pmatrix}\mathbf{v} + \mathbf{d}\\ \mathbf{k}(\mathbf{x}, t) - \frac{\mathbf{v}}{\kappa}\end{pmatrix}, \quad \tilde{\mathbf{J}}^* = \tilde{\mathbf{J}}, \quad \tilde{\mathbf{v}}_t^* = \begin{pmatrix}\mathbf{0}\\ \mathbf{k}_t - \nabla\mathbf{k}\cdot\mathbf{d}\end{pmatrix} . \tag{13}$$

The Jacobian $\tilde{\mathbf{J}}^* = \nabla\tilde{\mathbf{v}}^*$ and the time partial derivative of the high-dimensional flow $\tilde{\mathbf{v}}_t^* = \frac{\partial\tilde{\mathbf{v}}^*}{\partial t}$ follow directly by differentiation. Note that the calculation of the derivatives requires application of the chain rule, since with Eq. (1) position $\mathbf{x}$ is $\mathbf{x} = \mathbf{x}^* - \mathbf{c} - t\,\mathbf{d}$.

3.2 Inertial Motion in Steady Frame

To find the most-steady reference frame for inertial particle motion, Günther and Theisel [7] considered all smooth rotations and translations of the reference frame. The final vortex extraction eventually resulted in a parallel vectors operation in 6D. Since we concentrate in this paper on coreline shapes, we assume a Galilean transformation for simplicity. For the first-order criteria, this will result in a 3D parallel vectors problem that can be solved efficiently.

To find a steady reference frame, we rearrange the velocity subspace of Eq. (13) to select the translation parameter $\mathbf{d}$ for which the time partial of the high-dimensional flow $\tilde{\mathbf{v}}^*$ vanishes, i.e., $\tilde{\mathbf{v}}_t^* = \mathbf{0}$:

$$\boxed{\mathbf{d} = (\nabla\mathbf{k})^{-1}\mathbf{k}_t} . \tag{14}$$

When inserting Eq. (14) in Eq. (13), the flow becomes steady.

For the specific models from Eqs. (9) and (10) we get:

$$\text{Model 1}: \quad \mathbf{d} = \mathbf{J}^{-1}\,\mathbf{u}_t\ . \tag{15}$$

$$\text{Model 2}: \quad \mathbf{d} = \left(\mathbf{J} + \frac{3St}{2}\frac{\nabla D\mathbf{u}}{Dt}\right)^{-1}\left(\mathbf{u}_t + \frac{3St}{2}\frac{D^2\mathbf{u}}{Dt^2}\right)\ . \tag{16}$$

In case of Model 1, we have $\mathbf{d} = -\mathbf{f}$, where $\mathbf{f} = -\mathbf{J}^{-1}\mathbf{u}_t$ is the feature flow field [28] of massless particles, cf. Eq. (26) in [23]. Next, we extract inertial vortex corelines in the Galilean reference frame that is as steady as possible.

3.3 First-Order Corelines

3.3.1 2D Conditions

In the 2D steady vector fields of tracer particles, vortex centers are critical points with complex eigenvalues in the Jacobian [41]. Thus, for inertial flows we set $\tilde{\mathbf{v}}^* = \mathbf{0}$ in the high-dimensional inertial flow in Eq. (7). The position subspace gives a condition for $\mathbf{v}$, namely $\mathbf{v} = -\mathbf{d}$, which we insert in the velocity subspace, resulting in:

$$\mathbf{k} + \frac{\mathbf{d}}{\kappa} = \mathbf{0} \quad \Leftrightarrow \quad \boxed{\kappa\mathbf{k} + \mathbf{d} = \mathbf{0}} \quad \Leftrightarrow \quad \kappa(\nabla\mathbf{k})\mathbf{k} + \mathbf{k}_t = \mathbf{0}. \tag{17}$$

Inserting Model 1 from Eq. (9) or Model 2 from Eq. (10) into the boxed condition in Eq. (17) gives 2D conditions for locating the vortex center.

$$\text{Model 1}: \quad \mathbf{u} + r\,\mathbf{g} + \mathbf{d} = \mathbf{0}\,, \tag{18}$$

$$\text{Model 2}: \quad \mathbf{u} + \frac{3St}{2}\frac{D\mathbf{u}}{Dt} + \left(\frac{St}{R} - \frac{3St}{2}\right)\mathbf{g} + \mathbf{d} = \mathbf{0}\ . \tag{19}$$

To illustrate the above conditions, Fig. 1 shows space-time visualizations of the analytic Moving Center flow (cf. Eq. (44) in Section 5) for Model 1. In this flow, the vortex moves with constant speed over time, as illustrated by inertial pathlines (left). The motion results in a feature flow that is also constant and moves in the same direction as the coreline (right). Using line integral convolution (LIC), we visualize a slice of the vector field $\kappa\mathbf{k} + \mathbf{d}$, where 2D vortex centers can be found to obtain a seed point for the space-time tracking.

Space-Time Extraction. The above condition in Eq. (17) determines vortex centers for a given moment in time. By lifting the condition into space-time, the paths of vortex centers can be extracted at once using a parallel vectors operator [10]. In space-time, the following PV condition arises, where the last component is time:

$$\begin{pmatrix}\kappa\mathbf{k}\\ 1\end{pmatrix} \parallel \begin{pmatrix}-\mathbf{d}\\ 1\end{pmatrix}\ . \tag{20}$$

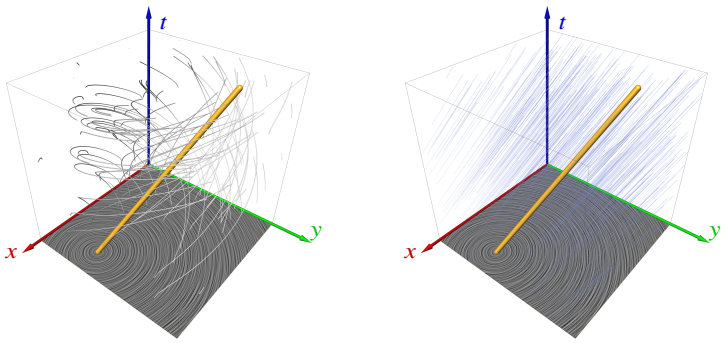

Fig. 1: *Inertial vortex coreline in the* Moving Center *flow for Model 1 using* $\mathbf{g} = (-2, 1)^{\mathrm{T}}$ *and* $r = 0.1$. *The flow* $\kappa\mathbf{k} + \mathbf{d}$ *is shown with a LIC slice at the bottom, and the coreline* (●) *shows the center of the vortex over time. Left, inertial pathlines* (●) *depict the behavior of inertial particles in the flow. Right, the ambient flow field* $\mathbf{d}$ (●) *is constant and evolves parallel to the vortex coreline.*

The space-time condition has interesting properties and can be reformulated as shown next. First, let $\bar{\mathbf{k}}$ be the vector field on the left side and let $\bar{\mathbf{K}} = \nabla\bar{\mathbf{k}}$ be its space-time Jacobian:

$$\bar{\mathbf{k}} = \begin{pmatrix} \kappa\mathbf{k} \\ 1 \end{pmatrix}, \qquad \bar{\mathbf{K}} = \left(\frac{\partial\bar{\mathbf{k}}}{\partial\mathbf{x}}, \frac{\partial\bar{\mathbf{k}}}{\partial t} \right) = \kappa \begin{pmatrix} \nabla\mathbf{k} & \mathbf{k}_t \\ \mathbf{0} & 0 \end{pmatrix}. \tag{21}$$

Since $\bar{\mathbf{K}} \begin{pmatrix} -\mathbf{d} \\ 1 \end{pmatrix} = \mathbf{0}$, we can see that $\begin{pmatrix} -\mathbf{d} \\ 1 \end{pmatrix}$ is an eigenvector of $\bar{\mathbf{K}}$ with the corresponding eigenvalue 0. With Eq. (20) it follows that on a vortex coreline, $\bar{\mathbf{k}}$ is also an eigenvector of $\bar{\mathbf{K}}$ and thus the reduced velocity criterion of Sujudi-Haimes [8] applies. When using the parallel vectors version [10] of the criterion on $\bar{\mathbf{k}}$, we get:

$$\kappa \begin{pmatrix} \nabla\mathbf{k} & \mathbf{k}_t \\ \mathbf{0} & 0 \end{pmatrix} \begin{pmatrix} \kappa\mathbf{k} \\ 1 \end{pmatrix} \parallel \begin{pmatrix} \kappa\mathbf{k} \\ 1 \end{pmatrix} \quad \Leftrightarrow \quad \boxed{\begin{pmatrix} \kappa(\nabla\mathbf{k})\mathbf{k} + \mathbf{k}_t \\ 0 \end{pmatrix} \parallel \begin{pmatrix} \kappa\mathbf{k} \\ 1 \end{pmatrix}}. \tag{22}$$

Note that the condition on the right can be computed without having to linearly solve for $\mathbf{d}$ in Eq. (14). The criterion on the right of Eq. (22) can only be fulfilled if its left side becomes zero, due to the time components (only the zero vector can be parallel to $\bar{\mathbf{k}}$). Thus, the following conditions are equivalent:

$$\mathbf{k} + \frac{\mathbf{d}}{\kappa} = \mathbf{0} \quad \Leftrightarrow \quad \kappa(\nabla\mathbf{k})\mathbf{k} + \mathbf{k}_t = \mathbf{0}. \tag{23}$$

The latter asks for the acceleration of vector field $\mathbf{k}$ to be zero.

3.3.2 3D Conditions

To find 3D corelines, we apply the method of Sujudi and Haimes [8] to the high-dimensional flow in the optimal steady frame, i.e., to $\tilde{\mathbf{v}}^*$ in Eq. (13). We search for locations at which the high-dimensional velocity $\tilde{\mathbf{v}}^*$ aligns with its acceleration:

$$\tilde{\mathbf{v}}^* \parallel \tilde{\mathbf{J}}^* \tilde{\mathbf{v}}^* \quad \Rightarrow \quad \begin{pmatrix} \mathbf{v} + \mathbf{d} \\ \mathbf{k} - \frac{\mathbf{v}}{\kappa} \end{pmatrix} \parallel \begin{pmatrix} \mathbf{k} - \frac{\mathbf{v}}{\kappa} \\ \nabla \mathbf{k} (\mathbf{v} + \mathbf{d}) - \frac{\mathbf{k} - \frac{\mathbf{v}}{\kappa}}{\kappa} \end{pmatrix} . \tag{24}$$

The above parallel vectors condition in Eq. (46) is six-dimensional and requires the search for both position and velocity. By requiring parallelism in the space subspace and the velocity subspace individually, the condition is simplified, since the dependence on the velocity $\mathbf{v}$ disappears, which was demonstrated for Model 1 [6]. In the Appendix 1, we show this for the general case, arriving at:

$$\boxed{\kappa \mathbf{k} + \mathbf{d} \parallel \nabla \mathbf{k} \, (\kappa \mathbf{k} + \mathbf{d})} \, , \tag{25}$$

which is now independent of the particle velocity $\mathbf{v}$. Thus, the parallel vectors condition in Eq. (25) can be searched in the position subspace using standard extractors, as introduced by Peikert and Roth [10]. Inserting Model 1 from Eq. (9) or Model 2 from Eq. (10) into Eq. (25) gives:

$$\text{Model 1 :} \quad \mathbf{u} + r\,\mathbf{g} + \mathbf{d} \quad \parallel \quad \mathbf{J} \, (\mathbf{u} + r\,\mathbf{g} + \mathbf{d}) \, , \tag{26}$$

$$\text{Model 2 :} \quad \mathbf{w} \parallel \left[\mathbf{J} + \frac{3St}{2} \nabla \left(\frac{D\mathbf{u}}{Dt} \right) \right] \mathbf{w} \, , \tag{27}$$

$$\text{with} \;\; \mathbf{w} = \mathbf{u} + \frac{3St}{2} \frac{D\mathbf{u}}{Dt} + \left(\frac{St}{R} - \frac{3St}{2} \right) \mathbf{g} + \mathbf{d} \, . \tag{28}$$

Note that Eq. (26) is the 3D condition that was derived by Günther and Theisel [6] (Eq. (32) in their paper for $\mathbf{d} = -\mathbf{f}$ as shown above), which appears here as special case.

Curvature of the Coreline. In the optimal steady reference frame, the condition $\tilde{\mathbf{v}}^* \parallel \tilde{\mathbf{J}}^* \tilde{\mathbf{v}}^*$ in Eq. (46) determines locations at which the high-dimensional flow is parallel to the acceleration. If both are parallel, the curvature of the resulting coreline vanishes. The curvature of a parameteric curve $\mathbf{x}(t)$ is given in any dimension by: $\kappa = \frac{\sqrt{\|\dot{\mathbf{x}}\|^2 \|\ddot{\mathbf{x}}\|^2 - (\dot{\mathbf{x}}^\mathrm{T} \ddot{\mathbf{x}})^2}}{\|\dot{\mathbf{x}}\|^3}$. The numerator vanishes if the enclosed angle θ between $\dot{\mathbf{x}}$ and $\ddot{\mathbf{x}}$ is zero, due to the dot product $\dot{\mathbf{x}}^\mathrm{T} \ddot{\mathbf{x}} = \|\dot{\mathbf{x}}\| \, \|\ddot{\mathbf{x}}\| \cos(\theta)$. In Eq. (46), we have velocity $\dot{\mathbf{x}} = \tilde{\mathbf{v}}^*$ and steady acceleration $\ddot{\mathbf{x}} = \tilde{\mathbf{J}}^* \tilde{\mathbf{v}}^*$. Thus, the first-order vortex coreline criterion models vortices as straight line structures.

3.4 Second-Order Corelines

Roth and Peikert [9] introduced an extension of Sujudi and Haimes [8] that models bent vortex corelines. Applied to our high-dimensional vector field in the optimal steady reference frame, vortex corelines are identified as locations that fulfill:

$$\tilde{\mathbf{v}}^* \parallel \tilde{\mathbf{b}}^* \quad \text{with} \quad \tilde{\mathbf{b}}^* = \frac{D}{Dt}(\tilde{\mathbf{J}}^*\tilde{\mathbf{v}}^*) \,. \tag{29}$$

The acceleration $\tilde{\mathbf{a}}^*$ in the transformed reference frame is

$$\tilde{\mathbf{a}}^* = \frac{D\tilde{\mathbf{v}}^*}{Dt} = \tilde{\mathbf{J}}^*\tilde{\mathbf{v}}^* \;=\; \begin{pmatrix} \mathbf{k} - \frac{\mathbf{v}}{\kappa} \\ \nabla\mathbf{k}(\mathbf{v}+\mathbf{d}) + \frac{\mathbf{v}}{\kappa^2} - \frac{\mathbf{k}}{\kappa} \end{pmatrix} , \tag{30}$$

which follows from insertion of Eqs. (13) into the left hand side of Eq. (30). Computing the material derivative of Eq. (30) as $\tilde{\mathbf{b}}^* = \frac{D\tilde{\mathbf{a}}^*}{Dt} = (\nabla\tilde{\mathbf{a}}^*)\tilde{\mathbf{v}}^*$ gives that the change in acceleration $\tilde{\mathbf{b}}^*$ is:

$$\tilde{\mathbf{b}}^* = \begin{pmatrix} \nabla\mathbf{k}(\mathbf{v}+\mathbf{d}) + \frac{\mathbf{v}}{\kappa^2} - \frac{\mathbf{k}}{\kappa} \\ \nabla(\nabla\mathbf{k})(\mathbf{v}+\mathbf{d})(\mathbf{v}+\mathbf{d}) - \frac{\nabla\mathbf{k}}{\kappa}(\mathbf{v}+\mathbf{d}) + \nabla\mathbf{k}(\mathbf{k} - \frac{\mathbf{v}}{\kappa}) - \frac{\mathbf{v}}{\kappa^3} + \frac{\mathbf{k}}{\kappa^2} \end{pmatrix} , \tag{31}$$

with $\nabla(\nabla\mathbf{k})(\mathbf{v}+\mathbf{d}) = \frac{\partial(\nabla\mathbf{k})}{\partial x}\cdot(u+d_1) + \frac{\partial(\nabla\mathbf{k})}{\partial y}\cdot(v+d_2) + \frac{\partial(\nabla\mathbf{k})}{\partial z}\cdot(w+d_3)$ for $\mathbf{d} = (d_1, d_2, d_3)^{\mathrm{T}}$. With Eq. (29), this leads to the following parallel vectors problem:

$$\boxed{\begin{pmatrix} \mathbf{v}+\mathbf{d} \\ \mathbf{k} - \frac{\mathbf{v}}{\kappa} \end{pmatrix} \parallel \begin{pmatrix} \nabla\mathbf{k}(\mathbf{v}+\mathbf{d}) + \frac{\mathbf{v}}{\kappa^2} - \frac{\mathbf{k}}{\kappa} \\ \nabla(\nabla\mathbf{k})(\mathbf{v}+\mathbf{d})(\mathbf{v}+\mathbf{d}) - \frac{\nabla\mathbf{k}}{\kappa}(\mathbf{v}+\mathbf{d}) + \nabla\mathbf{k}(\mathbf{k} - \frac{\mathbf{v}}{\kappa}) - \frac{\mathbf{v}}{\kappa^3} + \frac{\mathbf{k}}{\kappa^2} \end{pmatrix}} \tag{32}$$

This is a 6D parallel vectors problem, since both position $\mathbf{x}$ (for the evaluation of $\mathbf{k}$) and velocity $\mathbf{v}$ need to be searched. The extraction algorithm is described in Section 4.

4 Implementation

In the following, we explain the numerical extraction algorithms used to locate inertial critical points and inertial vortex corelines.

First-order Method. To find inertial critical points in 2D according to Eq. (17), we use the numerical subdivision approach of Globus et al. [24]. The line-based extraction of inertial critical paths in 2D space-time in Eq. (20) and the first-order extraction of inertial 3D corelines in Eq. (25) are formulated as 3D parallel vectors problems [10]. We used a Bézier-based subdivision to find the roots of the cross product [42, 43], which we refined using Newton iterations [44]. Several other existing algorithms would also be applicable [10, 45].

Second-order Method. The second-order method requires a 6D parallel vectors extraction in a 6D space. Recently, Hofmann and Sadlo [46] introduced the dependent vectors operator which extends the parallel vector operator to arbitrary dimensions, where our 6D PV problem is a special case. While their method provides a general framework for high dimensional features, their proposed algorithm does not scale well for our problem. The direct computation of the two 6D vector fields in Eq. (32) is too expensive, both in terms of computation time and memory consumption. To solve this problem, we follow the approach of Günther and Theisel [7], which we adapt to our vector configuration.

By writing the position subspace and the velocity subspace of Eq. (32) as functions in $\mathbf{v}$, we can simplify the search. By introducing the spatially-varying 3D vector fields $\underline{\mathbf{a}}$, $\underline{\mathbf{b}}$, $\underline{\mathbf{c}}$, $\underline{\mathbf{d}}$, matrix fields $\underline{\mathbf{B}}$, $\underline{\mathbf{C}}$, $\underline{\mathbf{D}}$, and tensor field $\underline{\underline{\mathbf{D}}}$, we can calculate the 6D vectors in Eq. (32) for a certain $\mathbf{v}$ on demand using only data stored in 3D:

$$\tilde{\mathbf{v}}^* \parallel \tilde{\mathbf{b}}^* \quad \Leftrightarrow \quad \begin{pmatrix} \mathbf{v} + \underline{\mathbf{a}} \\ \underline{\mathbf{B}}\,\mathbf{v} + \underline{\mathbf{b}} \end{pmatrix} \parallel \begin{pmatrix} \underline{\mathbf{C}}\,\mathbf{v} + \underline{\mathbf{c}} \\ \underline{\underline{\mathbf{D}}}\mathbf{v} \cdot (\mathbf{v} + \underline{\mathbf{a}}) + \underline{\mathbf{D}}\,\mathbf{v} + \underline{\mathbf{d}} \end{pmatrix}, \tag{33}$$

with the vector fields, matrix fields and tensor field:

$$\underline{\mathbf{a}} = \mathbf{d}\,, \qquad \underline{\mathbf{b}} = \mathbf{k}\,, \tag{34}$$

$$\underline{\mathbf{c}} = \nabla\mathbf{k} \cdot \mathbf{d} - \frac{\mathbf{k}}{\kappa}\,, \qquad \underline{\mathbf{C}} = \nabla\mathbf{k} + \frac{1}{\kappa^2}\mathbf{I}\,, \tag{35}$$

$$\underline{\mathbf{d}} = \nabla(\nabla\mathbf{k})\mathbf{d} \cdot \mathbf{d} - \frac{\nabla\mathbf{k}\mathbf{d}}{\kappa} + \nabla\mathbf{k}\mathbf{k} + \frac{\mathbf{k}}{\kappa^2}\,, \qquad \underline{\mathbf{B}} = -\frac{1}{\kappa}\mathbf{I}\,, \tag{36}$$

$$\underline{\mathbf{D}} = \nabla(\nabla\mathbf{k})\mathbf{d} - \frac{2\nabla\mathbf{k}}{\kappa} - \frac{1}{\kappa^3}\mathbf{I}\,, \qquad \underline{\underline{\mathbf{D}}} = \nabla(\nabla\mathbf{k})\,. \tag{37}$$

In practice, we discretize the above fields onto a piecewise linear tetrahedral 3D grid. At three spatial grid points $\mathbf{x}_i$ with $i \in \{1,2,3\}$ of a triangle, we therefore have the quantities $\underline{\mathbf{a}}_i$, $\underline{\mathbf{b}}_i$, $\underline{\mathbf{c}}_i$, $\underline{\mathbf{d}}_i$, $\underline{\mathbf{B}}_i$, $\underline{\mathbf{C}}_i$, $\underline{\mathbf{D}}_i$ and $\underline{\underline{\mathbf{D}}}_i$, which can be linearly interpolated with the barycentric weights a, b, c, subject to $a + b + c = 1$:

$$\underline{\mathbf{a}} = a\,\underline{\mathbf{a}}_1 + b\,\underline{\mathbf{b}}_2 + c\,\underline{\mathbf{c}}_3\,, \tag{38}$$

$$\underline{\mathbf{b}} = a\,\underline{\mathbf{b}}_1 + b\,\underline{\mathbf{b}}_2 + c\,\underline{\mathbf{b}}_3\,, \tag{39}$$

$$\vdots \tag{40}$$

$$\underline{\underline{\mathbf{D}}} = a\,\underline{\underline{\mathbf{D}}}_1 + b\,\underline{\underline{\mathbf{D}}}_2 + c\,\underline{\underline{\mathbf{D}}}_3\,. \tag{41}$$

At the same time, the velocity subspace is discretized onto a tetrahedral grid, for which we likewise assume barycentric interpolation with barycentric weights d, e, f, g inside the tetrahedra, subject to $d + e + f + g = 1$:

$$\mathbf{v} = d\,\mathbf{v}_1 + e\,\mathbf{v}_2 + f\,\mathbf{v}_3 + g\,\mathbf{v}_4\,. \tag{42}$$

Thus, the 6D PV condition $\tilde{\mathbf{v}}^* \parallel \tilde{\mathbf{b}}^*$ in Eq. (33) can now be expressed with Eqs. (36)–(42) in barycentric coordinates $(a, \ldots, g)$. To search the entire 6D space, each pair of position triangle and velocity tetrahedra must be tested. The PV solutions are points on the position triangles, which are connected to 3D lines in a post-process.

Two 6D vector fields $\tilde{\mathbf{v}}$ and $\tilde{\mathbf{w}}$ are parallel iff in generalization of the cross product the anti-symmetric matrix $\tilde{\mathbf{X}}$ is zero, with

$$\tilde{\mathbf{v}} \parallel \tilde{\mathbf{w}} \quad \Leftrightarrow \quad \tilde{\mathbf{X}} = \mathbf{0}_{6\times 6} \quad \text{with} \quad \tilde{\mathbf{X}}_{i,j} = \tilde{\mathbf{u}}_i \, \tilde{\mathbf{w}}_j - \tilde{\mathbf{w}}_i \, \tilde{\mathbf{u}}_j, \tag{43}$$

and the element indices $i, j \in \{1, \ldots, 6\}$. Thus, the search for parallel vectors becomes a root finding problem in all entries of matrix $\tilde{\mathbf{X}}$, which is quadratic in barycentric coordinates $\tilde{\mathbf{X}}(a, b, c; d, e, f, g)$.

After converting matrix $\tilde{\mathbf{X}}$ into Bernstein-Bezier form [42, 43], we use the convex hull property to quickly decide whether a root may exist inside a pair of position triangle and velocity tetrahedron. The conversion into Bernstein-Bezier form was described by Günther and Theisel [7], and we refer to their implementation section for the details. If a solution could exist in a tested pair, they performed a recursive subdivision, similar to Oster et al. [51], until the solution was found numerically. Their computation time is in the order of multiple hours. To speed up convergence, we instead use multi-variate Newton iterations [44] to locate the barycenteric coordinate at which the matrix $\tilde{\mathbf{X}}$ vanishes. After uniformly scaling the linear 6D vector fields $\tilde{\mathbf{v}}$ and $\tilde{\mathbf{w}}$ such that the longest vector has unit length, we iteratively minimize the Frobenius norm of $\tilde{\mathbf{X}}$. Since we do not recursively subdivide, significantly less pairs of triangles and tetrahedra need to be tested. For example, the computation time in the Vortex Ring at an initial spatial resolution of 32^3 voxels reduces from 70 *min* to 1.5 *min*. In pratice, we use higher grid resolutions, as shown later in Table 1, as our algorithm assumes linear interpolation on the tetrahedral elements covering the voxels of the grid. Note however that Newton iterations will only find one solution and can miss others if there a multiple solutions on the face of a cell. It should therefore only be applied when the bilinear face of a voxel is small enough, either because the initial grid resolution is fine enough, or after a certain number of recursive subdivisions have been performed. Our implementation of the multi-variate Newton iterations does not include further optimizations, such as line search or relaxation. Thus, there is room for further performance improvements.

5 Results

In the following, we test our extractors in several 2D and 3D flows, both analytic and numerical. For each experiment, we specify the inertial parameters as well as the applied extraction methods, that is, first-order or second-order coreline extraction.

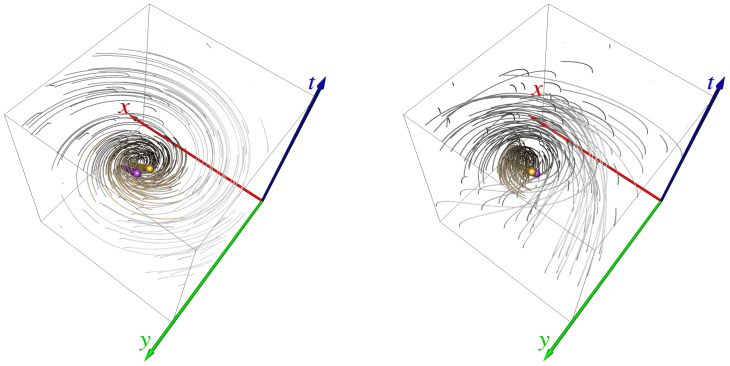

Fig. 2: *Inertial* (●) *and massless* (●) *vortex coreline in the* Moving Center *flow for Model 2 using* $\mathbf{g} = (0,2)^{\mathrm{T}}$. *On the left,* $R = 0.5$ *and* $St = 0.1$, *which models the behavior of aerosols such as sand particles in air. On the right,* $R = 0.7$ *and* $St = 0.7$, *which models the motion of bubbles. The corelines show the center of the vortex, while inertial pathlines* (●) *depict the overall movement of particles, showing that inertial particles close to the coreline revolve around the inertial vortex.*

5.1 Comparison of Inertial Particle Parameters

The first 2D flow contains a vortex center translating with constant speed along a straight line over time [27]:

$$\mathbf{u}(x,y,t) = \begin{pmatrix} -y + \frac{t}{2} - 1 \\ x + \frac{t}{2} - 1 \end{pmatrix}. \tag{44}$$

We consider the vector field in the space-time domain $D \times T = [-2,2]^2 \times [0,4]$. Fig. 2 shows the effect of the parameters St and R on the vortex position for Model 2, showing the behavior of both aerosols and bubbles. Pathlines (●) close to the vortex center (●) revolve around it over time, which indicates that the coreline extraction is accurate. In contrast to massless flows, inertial pathlines seeded from the coreline do not necessarily stay exactly on the coreline due to the inertia that carries them outward. Nevertheless, the general motion around the coreline can be observed.

5.2 Comparison of Inertial Particle Models

Cylinder Flow in 2D. The numerical 2D Cylinder flow contains a von-Kármán vortex street in the wake of an obstacle. The viscous fluid was injected from the left into a channel bounded by solid walls with a slip boundary condition. Fig. 3 shows two examples of Model 1 and 2 applied to this flow. In both cases, the symmetric flow creates translating vortices that remain coherent over time, which is visible in

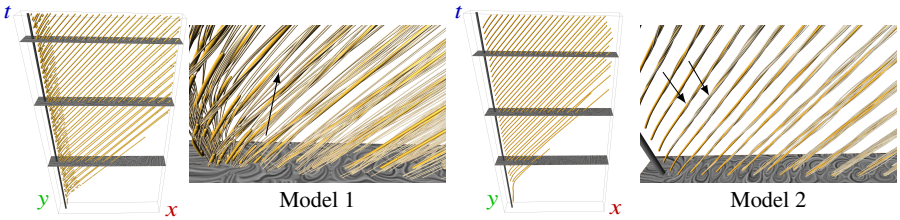

Fig. 3: *Inertial vortex corelines in the* Cylinder *flow for Model 1 (left) and 2 (right) using* $\mathbf{g} = (0, 1)^{\mathrm{T}}$, $r = 0.05$, $R = 2/3$ *and* $St = 0.01$. *Inertial pathlines* (●) *show that particles rotate around inertial corelines* (●)*, giving evidence of correctness.*

the space-time overview of the corelines (top). Depending on the particle model parameters, inertial particles can get trapped in the vortices while they are rotating around the corelines over time, which is visualized with inertial pathlines in the zoomed images. It becomes apparent that aerosol trajectories of Model 1 spiral away from the corelines, whereas the smaller neutrally buoyant particles of Model 2 remain close to their coreline. For this data set, the behavior of different inertial model parameters has previously been studied by Baeza Rojo et al. [47]. In our work, we automatically extract the vortex corelines, which compactly summarizes the loci of rotating motion.

Delta Wing in 3D. This numerical 3D flow was provided by Markus Rütten and contains a simulation of a triangular surface in upstream flow that generates two large wake vortices. We used a gravity-free environment, i.e., $\mathbf{g} = \mathbf{0}$, to extract a set of vortex corelines for both particle models. Fig. 4 shows the difference between Model 1 and Model 2. Although the location of vortex corelines is similar here, Model 1 trajectories exhibit significantly more inertia when using a response time of $r = 0.01$, compared to trajectories in Model 2 when using $R = 0.1$ and $St = 0.001$ as parameters. The Model 2 particles are smaller and thus follow the flow more tangentially than the Model 1 particles. Similar to the massless case, inertial particles of Model 2 revolve very closely around the vortex corelines.

Square Cylinder in 3D. This 3D unsteady fluid flow sequence shows the development of a von-Kármán vortex street. The obstacle, which is a squared cylinder, is positioned between two parallel walls, producing a periodic shedding of vortices over time. Fig. 5 shows selected frames of an accompanying animation, where we can see how inertial particles rotate around the extracted corelines. The heavy particles in Model 1 are affected by gravity, which drags particles down. The inertial vortex corelines (●) are shifted horizontally compared to the massless case (●) towards the updraft direction of the vortex, since this is where gravity cancels to zero. The shift therefore depends on the rotation direction of the vortex. Particles from Model 2, on the other hand, resemble bubbles (i.e., they have lower density than the liquid) and thus slowly rise up. It is also apparent that the behavior of particles in and around the vortices differs, since the inertia of particles of Model 1 carries particles further out. The low particle density inside vortices is characteristic for aerosol particles.

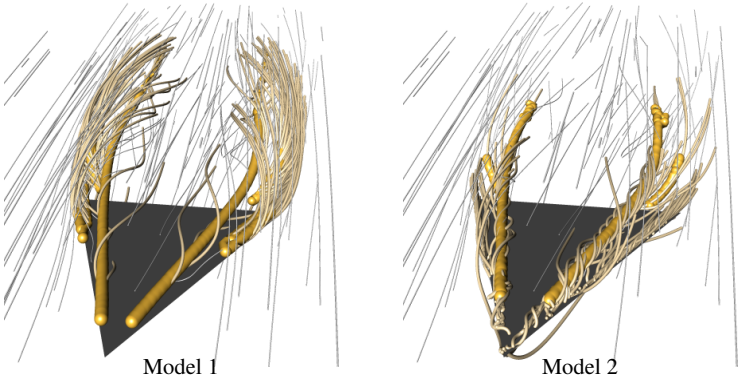

Fig. 4: *Inertial vortex corelines for model 1 (left) and 2 (right) in the* Delta Wing *using* $\mathbf{g} = (0,0,0)$*,* $r = 0.01$*,* $R = 0.1$ *and* $St = 0.001$*.*

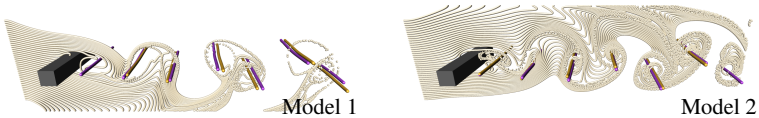

Fig. 5: *Comparison of inertial (●) and massless (●) vortex corelines in the flow behind a* Square Cylinder *for Model 1 (top,* $r = 0.25$*) and Model 2 (bottom,* $R = 0.8$ *and* $St = 0.4$*). The heavy aerosol particles of Model 1 are dragged down by gravity* $\mathbf{g} = (0,-1,0)$ *while the parameters of Model 2 represent bubbles, which rise upward.*

5.3 Second-order Corelines in 3D

Vortex Ring. Our next vector field contains a translating Vortex Ring, which serves as synthetic test case for the second-order extractor. The velocity magnitude along the coreline is denoted by s and the vortex translates with speed a along the z-axis.

$$\mathbf{u}(x,y,z,t) = \begin{pmatrix} -x \cdot (z + a \cdot t) - s \cdot y \\ -y \cdot (z + a \cdot t) + s \cdot x \\ x^2 + y^2 - 1 - a \end{pmatrix}. \tag{45}$$

In our examples, we set $a = s = 1$. We consider the flow in the spatial domain $[-2,2]^3$. In this flow, the vortex coreline is bent and thus the first-order methods fail to detect the correct coreline (●), as shown in Fig. 6. For the given model parameterization, the inertial particles of Model 1 exhibit more inertia than the particles in Model 2, leading them onto wider paths. The second-order vortex corelines (●) of both models are similar to each other. Note that the first-order criterion gives a wrong solution, since the coreline is not straight, which shows the necessity of our second-order vortex coreline criterion. Particles seeded on a vortex coreline are expected to remain close to the coreline over time, which is the case for our second-order condition.

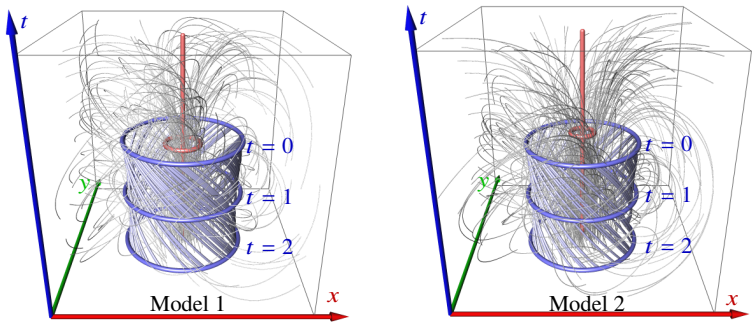

Fig. 6: *Bent second-order inertial vortex corelines in the* VORTEX RING *data set for Model 1 (left,* $r = 0.1$*) and Model 2 (right,* $R = 0.8$ *and* $St = 0.1$*) using* $\mathbf{g} = (0, 0, -1)$*. The second-order corelines* (●) *are shown for three different time steps, and the first-order corelines* (●) *for* $t = 0$*. Note that inertial pathlines* (●) *remain near the vortex over time, while inertial pathlines* (●) *from* $t = 0$ *show the rotating motion.*

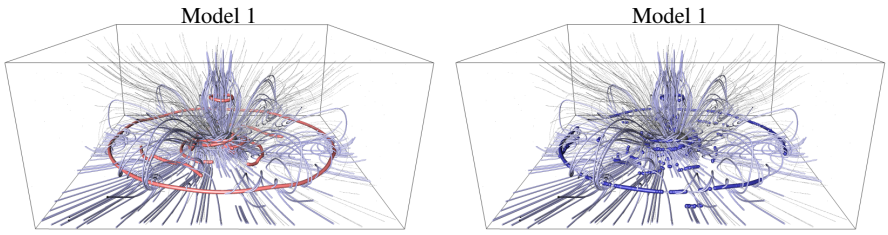

Fig. 7: *First-order* (●) *(left) and second-order* (●) *(right) inertial vortex corelines in the* HELICOPTER *data set for Model 1 using* $\mathbf{g} = \mathbf{0}$ *and* $r = 0.001$*. Near the ground, a large vortex ring forms around the hovering helicopter. The trajectories show the paths of sand particles. Differences between the methods can be seen below the rotor.*

Helicopter. Our last numerical example stems from brown-out engineering [1, 2], which studies the uplift of dust and sand when helicopters or airplanes approach the ground. The simulation shown in Fig. 7 contains a model rotor spinning at 75 Hz. The strong vertical airflow pushes down onto the sediment bed, as it carries tip vortices from the rotor into the domain. Due to numerical dissipation, these vortices are not well preserved in the simulation data. Very well distinguishable, however, is the large vortex ring that forms around the helicopter. The first-order and second-order corelines agree for this ring, since the velocity component along the vortex coreline is zero. There, particles are not moving along the vortex coreline, but stay stationary on it. Studying this intrinsically curved vortex is important, since it is a strong driver of sediment uplift, which causes mechanical wear of the blades and, more importantly, a limited view that frequently causes accidents. Differences between the two methods can be seen in the flow regime below the rotor blades, where the vortex coreline spirals outwards. These vortices eventually reach the sediment bed, causing uplift. Further, we can see that the second-order lines are more spurious than the first-order lines, which is a consequence of the numerical challenges of higher-order methods.

5.4 Memory Consumption and Performance

For all performance measurements, we used an Intel i7-6700K CPU with 32 GB RAM. All presented feature definitions are local and their extraction can thus easily be parallelized. In unsteady 2D flows, we only have to compute a 2D vector field in which the critical points are searched. This sums up to $2N$ double variables, where N is the number of grid points. Note that the time slices can be processed sequentially, which is why we only need to store a single time slice at a time. In 3D, we store for the first-order method two 3D vector fields, i.e., $6N$ double variables. For the 3D second-order methods, we store for each grid point 4 vector fields (a,b,c,d), 3 matrix fields (B,C,D) and 1 tensor field. This accumulates to $66N$ double variables. In general, the extraction performance is linear in the number of voxels that are tested for parallel vectors. The number of tested voxels depends on the amount and extent of swirling motion in the domain. The computation time of the quantities resulting in the vortex criterion and of the actual numerical extraction of the corelines are listed in Table 1. While the 2D and first-order 3D extraction can be carried out in the order of seconds (similar to the traditional massless case), the second-order 6D extraction is computationally still expensive, taking multiple hours on numerical data. Further speed-up could be achieved by pruning the search space, e.g., by considering only visible voxels in the domain or by specifying a region-of-interest, which have both not been implemented yet.

5.5 Discussion

Parameters. A benefit of our Galilean-invariant method, compared to the objective approach of Günther and Theisel [7], is that our reference frame optimization is parameter-free. While the objective method required the specification of a neighborhood region to regularize a linear system, the Galilean invariant approach has a local analytic solution.

Temporal Coherence. Our coreline definitions are local and do not involve any spatial or temporal smoothing kernels. Consequentially, temporal coherence is not directly enforced, which can result in temporal flickering. This is a general limitation of local methods [27, 6]. Obtaining smoother results is typically achieved through a pre-processing or post-processing step, which are orthogonal problems to the feature definition.

Computation Time. By using an iterative Newton refinement, the computation time of the 6D parallel vectors extraction reduced by about factor 40 compared to the Bézier-based subdivision in previous work [7], but it can still see improvements. An implicit or view-dependent computation of the line structures or a smarter selection of numerical parameters might be paths to faster updates.

		Grid	Memory	Order	M	VF	PV
Moving Center	2D	$128 \times 128 \times 128$	256 KB	1^{st}	1	0.11	0.30
					2	9.12	13.27
Cylinder	2D	$640 \times 80 \times 1501$	800 KB	1^{st}	1	13.74	2.61
					2	80.67	2.73
Squared Cylinder	3D	$192 \times 64 \times 48$	27 MB	1^{st}	1	0.55	6.74
					2	3.82	14.11
Delta Wing	3D	$250 \times 125 \times 100$	35.2 MB	1^{st}	1	2.47	0.07
					2	16.36	0.77
Vortex Ring	3D	$128 \times 128 \times 128$	96 MB	1^{st}	1	0.59	0.30
					2	0.74	0.26
			1.03 GB	2^{nd}	1	0.48	0.85 h
					2	0.82	1.1 h
Helicopter	3D	$128 \times 256 \times 256$	384 MB	1^{st}	1	8.25	1.37
			4.12 GB	2^{nd}	1	11.18	14 h

Table 1: *Computation time in seconds for the vector fields (VF) from Eq.* (20) *for first order space-time 2D, Eq.* (25) *for 3D and Eq.* (32) *for second order and corelines extraction with parallel vectors (PV) for the two models (M).*

Reference Frame Invariance. The shape of a coreline and its motion are two independent phenomena. In fact, in the Vortex Ring data set in Fig. 6, the objective approach [7] and the first-order Galilean-invariant method [6] will both give an identical (and wrong) result, since the vortex ring is not straight and performs an equal-speed translation. In this paper, we introduced a criterion to extract more general inertial coreline shapes. For this, we concentrated on vortex corelines that perform Galilean transformations. To handle more arbitrary motions in the future, we would like to apply the second-order criterion in reference frames that are objective.

Limit Case for Tracer Particles. A natural question that arises for feature definitions of inertial particles is whether they are consistent with the massless case. In the Appendix 2, we show that our inertial first-order and second-order criteria approach the massless case in the limit for $\kappa \to 0$, as desired.

6 Conclusion

In this paper, we developed vortex coreline extractors for inertial particles for two particle models. Based on the selection of an optimal Galilean reference frame, in which the flow field becomes steady, we introduced generalized coreline criteria that include both particle models as special cases. After covering the 2D case, we discussed the first-order and second-order inertial coreline extraction in 3D, which required a 3D or 6D parallel vectors extraction. For the latter, we combined a Bézier-based subdivision approach with a subsequent iterative Newton refinement. Our work connects to reference frame optimization, shedding light on the formal mathematical properties of previous work [6] that derived a criterion geometrically.

Acknowledgements The Cylinder flow was numerically simulated with Gerris Flow solver [48], The Delta Wing vector field was kindly provided by Markus Rütten and the Square Cylinder flow was simulated by Camarri et al. [49] and resampled by Tino Weinkauf. The Helicopter flow was simulated by Benjamin Kutz [3]. For all visualizations, we used Amira [50]. This work was supported by the Swiss National Science Foundation (SNSF) Ambizione grant no. PZ00P2_180114 and by ETH Research Grant ETH-07 18-1.

Appendix 1 - Derivation of First-order 3D Criterion

Next, we show how the 6D parallel vectors condition of the first-order case:

$$\tilde{\mathbf{v}}^* \parallel \tilde{\mathbf{J}}^* \tilde{\mathbf{v}}^* \quad \Rightarrow \quad \begin{pmatrix} \mathbf{v}+\mathbf{d} \\ \mathbf{k}-\frac{\mathbf{v}}{\kappa} \end{pmatrix} \parallel \begin{pmatrix} \mathbf{k}-\frac{\mathbf{v}}{\kappa} \\ \nabla\mathbf{k}(\mathbf{v}+\mathbf{d}) - \frac{\mathbf{k}-\frac{\mathbf{v}}{\kappa}}{\kappa} \end{pmatrix} . \tag{46}$$

can be simplified to a 3D criterion. First, we look at the position subspace. Multiplying with κ and adding $\mathbf{v}+\mathbf{d}$ to the right hand side gives:

$$\mathbf{v}+\mathbf{d} \parallel \mathbf{k}-\frac{\mathbf{v}}{\kappa} \quad \Leftrightarrow \quad \mathbf{v}+\mathbf{d} \parallel \kappa\mathbf{k}-\mathbf{v} \tag{47}$$

$$\Leftrightarrow \quad \mathbf{v}+\mathbf{d} \parallel \kappa\mathbf{k}+\mathbf{d}, \tag{48}$$

Equating Eq. (47) and Eq. (48) gives:

$$\mathbf{k}-\frac{\mathbf{v}}{\kappa} \parallel \kappa\mathbf{k}+\mathbf{d}. \tag{49}$$

Considering the velocity subspace of Eq. (46):

$$\mathbf{k}-\frac{\mathbf{v}}{\kappa} \parallel \nabla\mathbf{k}\,(\mathbf{v}+\mathbf{d}) - \frac{\mathbf{k}-\frac{\mathbf{v}}{\kappa}}{\kappa} , \tag{50}$$

and multiplying the right hand side with κ gives:

$$\mathbf{k}-\frac{\mathbf{v}}{\kappa} \parallel \kappa\nabla\mathbf{k}\,(\mathbf{v}+\mathbf{d}) - \mathbf{k} + \frac{\mathbf{v}}{\kappa} . \tag{51}$$

Adding the left hand side to the right hand side and dividing by κ:

$$\mathbf{k}-\frac{\mathbf{v}}{\kappa} \parallel \nabla\mathbf{k}\,(\mathbf{v}+\mathbf{d}). \tag{52}$$

Finally, substituting Eq. (49) on the left hand side of Eq. (52) and inserting Eq. (48) on the right hand side of Eq. (52) gives Eq. (25):

$$\kappa\mathbf{k}+\mathbf{d} \parallel \nabla\mathbf{k}\,(\kappa\mathbf{k}+\mathbf{d}) , \tag{53}$$

which is a 3D condition, independent of the particle velocity $\mathbf{v}$.

Appendix 2 - Tracer Particles as Limit Case

Next, we show that our inertial first-order and second-order criteria approach the massless case in the limit. The proofs of Model 1 and 2 are analogue. For brevity, we show the derivation for Model 1.

Inertial Motion. First, the motion of inertial particles is consistent with tracer particles for $r \to 0$, as shown by Günther and Theisel [6]: Rearranging the velocity subspace of $\tilde{\mathbf{v}}$ in Eq. (7) for $\mathbf{v}$ and substituting in the position subspace of $\tilde{\mathbf{v}}$ gives with Eq. (9):

$$\lim_{r\to 0} \frac{\mathrm{d}\mathbf{x}}{\mathrm{d}t} = \mathbf{v} = \mathbf{u}(\mathbf{x},t) \underbrace{-r\frac{\mathrm{d}\mathbf{v}}{\mathrm{d}t} + r\mathbf{g}}_{0} \,. \tag{54}$$

Vortex Centers in 2D. The motion of inertial particles is described with Eq. (9). We consider the limit $r \to 0$ for tracer particles:

$$\kappa = r \qquad \kappa\mathbf{k} = \mathbf{u}(\mathbf{x},t) + r\mathbf{g} \tag{55}$$

$$\lim_{r\to 0} \kappa\mathbf{k} = \mathbf{u}(\mathbf{x},t) \,. \tag{56}$$

With $\mathbf{d} = \mathbf{J}^{-1}\mathbf{u}_t = -\mathbf{f}$ from Eq. (15), we insert the limit in Eq. (56) into the general 2D vortex center condition in Eq. (17):

$$\kappa\mathbf{k} + \mathbf{d} = \mathbf{0} \qquad \overset{r\to 0}{\Rightarrow} \qquad \mathbf{u}(\mathbf{x},t) - \mathbf{f} = \mathbf{0}, \tag{57}$$

which is the Galilean invariant 2D vortex coreline criterion for massless particles by Weinkauf et al. [27], cf. Eq. (55) in [23].

First-order Corelines in 3D. For the first-order vortex corelines in 3D, we insert the limit in Eq. (56) into the general first-order vortex coreline condition in Eq. (25):

$$\kappa\mathbf{k} + \mathbf{d} \parallel \nabla\mathbf{k}\,(\kappa\mathbf{k} + \mathbf{d}) \qquad \overset{r\to 0}{\Rightarrow} \qquad \mathbf{u} - \mathbf{f} \parallel \frac{\mathbf{J}}{r}\,(\mathbf{u} - \mathbf{f}) \tag{58}$$

$$\mathbf{u} - \mathbf{f} \parallel \mathbf{J}\,(\mathbf{u} - \mathbf{f})\,, \tag{59}$$

which is the Galilean invariant first-order 3D vortex coreline criterion for massless particles by Weinkauf et al. [27], cf. Eq. (53) in [23].

Second-order Corelines in 3D. We consider the transformed velocity $\tilde{\mathbf{v}}^*$ in Eq. (13) and the rate of acceleration $\tilde{\mathbf{b}}^*$:

$$\tilde{\mathbf{b}}^* = \begin{pmatrix} \nabla\mathbf{k}(\mathbf{v}+\mathbf{d}) + \frac{\mathbf{v}}{\kappa^2} - \frac{\mathbf{k}}{\kappa} \\ \nabla(\nabla\mathbf{k})(\mathbf{v}+\mathbf{d})(\mathbf{v}+\mathbf{d}) - \frac{\nabla\mathbf{k}}{\kappa}(\mathbf{v}+\mathbf{d}) + \nabla\mathbf{k}(\mathbf{k} - \frac{\mathbf{v}}{\kappa}) - \frac{\mathbf{v}}{\kappa^3} + \frac{\mathbf{k}}{\kappa^2} \end{pmatrix} \tag{60}$$

in the optimal reference frame, i.e., $\mathbf{d}$ is the translation rate:

$$\tilde{\mathbf{v}}^* = \begin{pmatrix} \mathbf{v}+\mathbf{d} \\ \mathbf{a}^* \end{pmatrix} . \qquad \tilde{\mathbf{b}}^* = \begin{pmatrix} \mathbf{b}^* \\ \mathbf{c}^* \end{pmatrix} . \tag{61}$$

We rearrange the velocity subspace in Eq. (60), denoted as $\mathbf{c}^*$ with

$$\mathbf{c}^* = \nabla(\nabla\mathbf{k})(\mathbf{v}+\mathbf{d})(\mathbf{v}+\mathbf{d}) - \frac{\nabla\mathbf{k}}{\kappa}(\mathbf{v}+\mathbf{d}) + \nabla\mathbf{k}(\mathbf{k} - \frac{\mathbf{v}}{\kappa}) - \frac{\mathbf{v}}{\kappa^3} + \frac{\mathbf{k}}{\kappa^2}$$

and with $\mathbf{a}^* = \mathbf{k} - \frac{\mathbf{v}}{\kappa} = \mathbf{J}(\mathbf{u}-\mathbf{f})$ [23] and $\mathbf{b}^*$ in Eq. (60) into

$$\mathbf{c}^* = \nabla(\nabla\mathbf{k})(\mathbf{v}+\mathbf{d})(\mathbf{v}+\mathbf{d}) + \nabla\mathbf{k}\,(\mathbf{J}(\mathbf{u}-\mathbf{f})) - \frac{\mathbf{b}^*}{\kappa}. \tag{62}$$

Inserting Model 1 with Eqs. (56) and (57) gives for $r \to 0$:

$$\mathbf{c}^* = \frac{1}{r}\nabla\mathbf{J}(\mathbf{u}-\mathbf{f})(\mathbf{u}-\mathbf{f}) + \frac{\mathbf{J}}{r}\,(\mathbf{J}(\mathbf{u}-\mathbf{f})) - \frac{\mathbf{b}^*}{r} \tag{63}$$

$$\Leftrightarrow\ r\cdot\mathbf{c}^* = \nabla\mathbf{J}(\mathbf{u}-\mathbf{f})(\mathbf{u}-\mathbf{f}) + \mathbf{J}\,(\mathbf{J}(\mathbf{u}-\mathbf{f})) - \mathbf{b}^* = \mathbf{0}. \tag{64}$$

Rearranging for the rate of acceleration $\mathbf{b}^*$ gives the material derivative of the steady acceleration $\frac{D}{Dt}(\mathbf{J}\mathbf{u}^*)$ in the optimal frame:

$$\lim_{r\to 0}\mathbf{b}^* = (\nabla\mathbf{J}\mathbf{u}^* + \mathbf{J}\mathbf{J})\,\mathbf{u}^* \quad \text{with} \quad \mathbf{u}^* = \mathbf{u}-\mathbf{f}\,. \tag{65}$$

Thus, the position subspace simplifies to $\mathbf{u}^* \parallel \mathbf{b}^*$, which is equivalent to the criterion of Roth and Peikert [9] in the optimal steady reference frame. Thus, all proposed inertial vortex criteria are consistent with the massless case for $r \to 0$.

References

1. Syal M., Govindarajan B., Leishman J. G.: Mesoscale sediment tracking methodology to analyze brownout cloud developments. In Proceedings of the American Helicopter Society, 66th Annual Forum (2010)
2. Sydney A., Baharani A., Leishman J. G.: Understanding brownout using near-wall dual-phase flow measurements. In Proceedings of the American Helicopter Society (Virginia Beach, VA, May 2011), 67th Annual Forum
3. Kutz B. M., Gunther T., Rumpf A., Kuhn A.: Numerical examination of a model rotor in brownout conditions. In Proceedings of the American Helicopter Society (2014), no. AHS2014–000343
4. Karl D. M.: A sea of change: Biogeochemical variability in the north pacific subtropical gyre. Ecosystems 2, 3 (May 1999), 181–214
5. Bordas R.: Optical measurements in disperse two-phase flows: Application to rain formation in cumulus clouds. PhD thesis, University of Magdeburg, 2011
6. Günther T., Theisel H.: Vortex cores of inertial particles. IEEE Transactions on Visualization and Computer Graphics (Proc. IEEE SciVis) 20, 12 (2014), 2535–2544

7. Günther T., Theisel H.: Objective vortex corelines of finite-sized objects in fluid flows. IEEE Transactions on Visualization and Computer Graphics (Proc. IEEE Scientific Visualization 2018) 25, 1 (2019), 956–966
8. Sujudi D., Haimes R.: Identification of Swirling Flow in 3D Vector Fields. Tech. rep., Departement of Aeronautics and Astronautics, MIT, 1995. AIAA Paper 95–1715
9. Roth M., Peikert R.: A higher-order method for finding vortex core lines. In Proc. IEEE Visualization (1998), 143–150
10. Peikert R., Roth M.: The "parallel vectors" operator – a vector field visualization primitive. In Proc. IEEE Visualization (1999), 263–270
11. Lugt H. J.: The dilemma of defining a vortex. Recent developments in theoretical and experimental fluid mechanics. Springer, 1979, 309–321
12. Robinson S. K.: Coherent motions in the turbulent boundary layer. Annual Review of Fluid Mechanics 23, 1 (1991), 601–639
13. Crowe C., Sommerfield M., Tsuji Y.: Multiphase Flows with Droplets and Particles. CRC Press, 1998
14. Haller G., Sapsis T.: Where do inertial particles go in fluid flows? Physica D: Nonlinear Phenomena 237 (May 2008), 573–583
15. Sudharsan M., Brunton S. L., Riley J. J.: Lagrangian coherent structures and inertial particle dynamics. ArXiv e-prints (2015). 1512.05733
16. Wan Z. Y., Sapsis T. P.: Machine learning the kinematics of spherical particles in fluid flows. Journal of Fluid Mechanics 857 (2018)
17. Benzi R., Biferale L., Calzavarini E., Lohse D., Toschi F.: Velocity-gradient statistics along particle trajectories in turbulent flows: The refined similarity hypothesis in the Lagrangian frame. Phys. Rev. E 80 (Dec 2009), 066318
18. Cartwright J. H. E., Feudel U., Karolyi G., Moura A., Piro O., Tel T.: Dynamics of finite-size particles in chaotic fluid flows. In Nonlinear Dynamics and Chaos: Advance and Perspectives, Thiel M., Kurths J., Romano M. C., Károlyi G., Moura A., (Eds.), Understanding Complex Systems. Springer Berlin Heidelberg, 2010, 51–87
19. Bec J., Biferale L., Cencini M., Lanotte A. S., Toschi F.: Spatial and velocity statistics of inertial particles in turbulent flows. Journal of Physics: Conference Series 333, 1 (2011), 012003
20. Benczik I. J., Toroczkai Z., Tel T.: Selective sensitivity of open chaotic flows on inertial tracer advection: Catching particles with a stick. Phys. Rev. Lett. 89 (Sep 2002), 164501
21. Babiano A., Cartwright J. H. E., Piro O., Provenzale A.: Dynamics of a small neutrally buoyant sphere in a fluid and targeting in Hamiltonian systems. Phys. Rev. Lett. 84 (Jun 2000), 5764–5767
22. Vilela R. D., de Moura A. P. S., Grebogi C.: Finite-size effects on open chaotic advection. Phys. Rev. E 73 (2006), 026302
23. Günther T., Theisel H.: The state of the art in vortex extraction. Computer Graphics Forum 37, 6 (2018), 149–173
24. Globus A., Levit C., Lasinski T.: A tool for visualizing the topology of threedimensional vector fields. In Proc. IEEE Visualization (1991), 33–40
25. Sahner J., Weinkauf T., Hege H.-C.: Galilean invariant extraction and iconic representation of vortex core lines. In Proc. Eurographics / IEEE VGTC Symposium on Visualization (EuroVis) (2005), 151–160
26. Fuchs R., Peikert R., Hauser H., Sadlo F., Muigg P.: Parallel vectors criteria for unsteady flow vortices. IEEE Transactions on Visualization and Computer Graphics 14, 3 (2008), 615–626
27. Weinkauf T., Sahner J., Theisel H., Hege H.-C.: Cores of swirling particle motion in unsteady flows. IEEE Transactions on Visualization and Computer Graphics (Proc. Visualization) 13, 6 (2007), 1759–1766
28. Theisel H., Seidel H.-P.: Feature flow fields. In Proc. Symposium on Data Visualisation (2003), 141–148
29. Günther T., Schulze M., Theisel H.: Rotation invariant vortices for flow visualization. IEEE Transactions on Visualization and Computer Graphics (Proc. IEEE SciVis 2015) 22, 1 (2016), 817–826

30. Günther T., Gross M., Theisel H.: Generic objective vortices for flow visualization. ACM Transactions on Graphics (Proc. SIGGRAPH) 36, 4 (2017), 141:1–141:11
31. Hadwiger M., Mlejnek M., Theuÿl T., Rautek P.: Time-dependent flow seen through approximate observer killing fields. IEEE Transactions on Visualization and Computer Graphics (Proceedings IEEE Scientific Visualization 2018) 25, 1 (2019), 1257–1266
32. Chong M. S., Perry A. E., Cantwell B. J.: Ageneral classification of three-dimensional flow fields. Physics of Fluids A: Fluid Dynamics 2, 5 (1990), 765–777
33. Baeza Rojo, I, Günther, T.: Vector Field Topology of Time-Dependent Flows in a Steady Reference Frame. IEEE Transactions on Visualization and Computer Graphics (Proc. IEEE Scientific Visualization 2019)
34. Günther T., Theisel H.: Hyper-objective vortices. IEEE Transactions on Visualization and Computer Graphics, 26, 3 (2020), 1532–1547
35. Wiebel A.: Feature Detection in Vector Fields Using the Helmholtz-Hodge Decomposition. Diploma thesis, Univ. Kaiserslautern, 2004
36. Wiebel A., Garth C., Scheuermann G.: Computation of localized flow for steady and unsteady vector fields and its applications. IEEE Transactions on Visualization and Computer Graphics 13, 4 (2007), 641
37. Bhatia H., Pascucci V., Kirby R. M., Bremer P.-T.: Extracting features from time-dependent vector fields using internal reference frames. Computer Graphics Forum (Proc. EuroVis) 33, 3 (2014), 21–30
38. Bujack R., Hlawitschka M., Joy K. I.: Topology-inspired Galilean invariant vector field analysis. In IEEE Pacific Visualization Symposium (April 2016), 72–79
39. Kim B., Günther T.: Robust reference frame extraction from unsteady 2D vector fields with convolutional neural networks. Computer Graphics Forum (Proc. EuroVis) 38, 3 (2019)
40. Günther T., Gross M.: Flow-induced inertial steady vector field topology. Computer Graphics Forum (Proc. Eurographics) 36, 2 (2017), 143–152
41. Helman J. L., Hesselink L.: Representation and display of vector field topology in fluid flow data sets. Computer 22, 8 (1989), 27–36
42. Rockwood A., Heaton K., Davis T.: Real-time rendering of trimmed surfaces. In ACM SIGGRAPH Computer Graphics (1989), vol. 23, ACM, 107–116
43. Hoschek J., Lasser D.: Fundamentals of Computer Aided Geometric Design. AK Peters, 1993
44. Kelley C. T.: Iterative methods for linear and nonlinear equations. Frontiers in applied mathematics 16 (1995), 575–601
45. Van Gelder A., Pang A.: Using PVsolve to analyze and locate positions of parallel vectors. IEEE Transactions on Visualization and Computer Graphics 15, 4 (2009), 682–695
46. Hofmann L., Sadlo F.: The Dependent Vectors Operator. Computer Graphics Forum (Proc. EuroVis) 38, 3 (2019), 261–272, doi:10.1111/cgf.13687
47. Baeza Rojo I., Gross M., Gunther T.: Visualizing the phase space of heterogeneous inertial particles in 2D flows. Computer Graphics Forum (Proc. EuroVis) 37, 3 (2018), 289–300
48. Popinet S.: Free computational fluid dynamics. Cluster World 2, 6 (2004)
49. Camarri S., Salvetti M.-V., Buffoni M., Iollo A.: Simulation of the three-dimensional flow around a square cylinder between parallel walls at moderate Reynolds numbers. In XVII Congresso di Meccanica Teorica ed Applicata (2005)
50. Stalling D., Westerhoff M., Hege H.-C.: Amira: A highly interactive system for visual data analysis. The Visualization Handbook. Elsevier, 2005, 749–767
51. Oster T., Rossl C., Theisel H.: Core lines in 3D second-order tensor fields. Computer Graphics Forum (Proc. EuroVis) 37, 3 (2018), 327–337